MTLA 32 (2023) 101911

Contents lists available at ScienceDirect

Materialia

journal homepage: www.elsevier.com/locate/mtla

Synchrotron X-ray diffraction analysis of constituent phases in transition joint between nickel alloy 738LC and a MnFeCoNiCu alloy

Benjamin Schneiderman [a], Andrew Chihpin Chuang [b], Zhenzhen Yu [a,*]

[a] George S. Ansell Department of Metallurgical and Materials Engineering, Colorado School of Mines, 1500 Illinois St, Golden, CO 80401, United States
[b] Advanced Photon Source, Argonne National Laboratory, 9700 S. Cass Ave, Lemont, IL 60439, United States

ARTICLE INFO

Keywords:
High entropy alloys
Complex concentrated alloys
Multi principal element alloys
Nickel-base superalloys
Phase identification
Synchrotron
X-ray diffraction
Hard sphere model
Laser welding

ABSTRACT

Synchrotron x-ray diffraction (XRD) analysis was performed on transition joints between a single-phase MnFeCoNiCu alloy and Ni-base Alloy 738LC to efficiently identify the constituent phases across the interface, with different levels of material intermixing generated by laser-welding with variable power. The intermixing extent was quantified by postmortem energy dispersive x-ray spectroscopy mapping. Diffraction-based analyses on complex composition spaces with limited prior data present significant challenges because elemental substitution in both disordered and ordered phases is more extensive than in conventional alloy spaces, which may effectuate relatively large shifts in the observed lattice parameters that convolute the analysis. Therefore, thermodynamic simulations and crystallographic literature data were employed to construct a system-specific diffraction library of twelve prospective phases for the composition space investigated. Subsequently, for predicted disordered cubic phases, statistical hard-sphere models were established to estimate the lattice parameters and predict diffraction peak positions for inclusion in the library. The library was then employed to analyze diffraction profiles measured from the variably intermixed transition joints, with focus on accounting for both high and low-intensity peaks. 99.0 % of diffraction peaks with relative intensity greater than 0.001 were assigned to phases from the system-specific library, exemplifying rigorous peak accounting and indicating that no unexpected phases were present. Up to six of the twelve library phases were experimentally found in the transition joints. The lattice parameters predicted by the statistical hard-sphere model based upon thermodynamic simulations agree reasonably well with the measured values for the disordered FCC matrix phase.

1. Introduction

Since they were conceptualized in 2004 [1,2], high-entropy alloys (HEAs) have been an area of interest in the metallurgical community because they comprise a vast space from which to design novel structural or functional materials. While the original entropy-driven postulates of HEAs laid important groundwork for research in this field, the universality of these effects across all HEA compositions has been called into question in recent studies [3,4]. Therefore, many researchers in materials design are shifting away from strict, entropy-based definitions and broadening the design space to include multi-principal element alloys (MPEAs) or complex, concentrated alloys (CCAs) [5]. In this broadened design space, concentration limits and restrictions on the number of constituent elements are more relaxed, such that many traditional material systems including Ni-superalloys and even some stainless steels meet criteria for classification as MPEAs or CCAs [5].

When investigating novel materials in the CCA design space, a thorough assessment of their constituent metallurgical phases is essential to understand performance. High energy synchrotron x-ray diffraction (XRD) is a powerful and efficient technique available for phase identification, combining the ability to assess relatively large material volumes and to detect low-volume-fraction constituents. Volume fractions as low as 0.0045 have reportedly been detected using this technique [6], with this detection limit depending on the experiment setup and the phases in question. Historically, phase identification from an XRD pattern was accomplished by comparison with the powder diffraction file [7,8], a comprehensive database of materials' powder diffraction patterns amassed over the past 80 years [9,10]. In recent decades, several software packages for automated phase identification using methods based on comparison to this database have been developed [10]. Moreover, the advent of diffraction pattern simulation from a crystal information file has enhanced flexibility in assessing structures

* Corresponding author.
E-mail address: zyu@mines.edu (Z. Yu).

https://doi.org/10.1016/j.mtla.2023.101911
Received 26 June 2023; Accepted 23 September 2023
Available online 24 September 2023

that are deviant from their exact stoichiometry. However, multiphase CCAs with limited prior data available nonetheless pose challenges in diffraction-based analyses. Many CCAs (e.g., novel MPEAs and established Ni-superalloy CCAs) are assessed in their as-cast state [5], where large grain size and strong solidification texture cause significant deviations from powder-pattern intensities. Additionally, disordered solid-solution phases common to CCAs often have lattice parameters and corresponding XRD peak positions that vary considerably from those of cubic phases in less concentrated alloy systems. Furthermore, any non-solid-solution phases that exist in CCA systems may differ from their known stoichiometry in isolation, due to the extensive availability of varied elements in the CCA for substitution, causing corresponding shifts in *d*-spacing for these phases as well. The commonly used Rietveld refinement technique [11] can accommodate deviations from powder intensities and known lattice constants by iteratively refining relevant parameters until the differences between an experimental pattern and that calculated from a set of input crystal structures are minimized. However, when assessing novel CCA materials, this technique is limited in that it requires each crystal structure to be input as a single unit cell, which cannot capture the disordered nature of random solid-solution structures common to many CCAs. Furthermore, this technique is best suited to refine strong peaks, as in a multiphase system where each phase comprises large volume fractions such 10 % or greater, as exemplified by Gasan et al. [12], but it may not capture low volume fraction constituents. Most critically, inputting a set of conventional, known phases in a novel alloy system creates the potential for incorrect phase identification if false assumptions regarding the present microconstituents are made.

These above-mentioned aspects render phase identification from XRD in CCA systems a challenging, complex undertaking that requires a multifaceted analysis, which is acknowledged in a few recent literature studies. For example, Gasan et al. discuss the necessity of using equilibrium and non-equilibrium thermodynamic simulations to compare and guide their quantitative Rietveld refinement results for a four-phase $Al_xCoCrFeMoNi$ CCA system [12]. This strategy can reduce the possibility of erroneous structure selection. Other studies compare experimental XRD data of a CCA to the predicted constituent phases from thermodynamic simulations [13,14]. However, few XRD studies on CCA systems discuss the extent of peak shifting resulting from elemental substitution to validate assigning experimental XRD peaks to a particular phase.

This work uses synchrotron XRD to investigate a complex joint structure transiting from a random solid-solution single phase $Mn_{35}Fe_5Co_{20}Ni_{20}Cu_{20}$ MPEA (composition approximate) [15–18] to the multiphase Ni-base Alloy 738LC, with different levels of intermixing at the interface generated by adjusting the input power when laser welding. This MnFeCoNiCu-type MPEA was developed as a joining filler for Ni-base superalloys for mitigation of weldability issues [15,16]. The MPEA/Alloy 738LC intermixed region is compositionally complex, as this intermixed region contains both refractory elements and precipitate-forming elements from Alloy 738LC, in addition to the five principal alloying element of MPEA [19,20]. A thorough understanding of the phase constituents in the joint structure as a function of intermixing level, especially the minor phases, is critical for understanding the resulting mechanical performance. In this study, thermodynamic simulations were firstly used to generate a system-specific phase library spanning the composition space, and statistical hard sphere models were employed to predict lattice parameters for the disordered solid solution phases predicted. The phase library then guided the indexing of both the high- and low-intensity XRD peaks collected from a synchrotron source. The deviations from stoichiometric peak positions caused by elemental substitution are discussed in detail in this work, providing additional rationalization for the peak assignment.

2. Simulations

The flowchart in Fig. 1 summarizes the workflow for assessing the constituent phases in the mixed-CCA composition space. In this work, the MnFeCoNiCu-type MPEA is treated as the filler material, Alloy 738LC is treated as the base, and any intermediate composition is treated as the weld. To label the range of intermediate compositions between the MnFeCoNiCu-type MPEA and Alloy 738LC, a dilution parameter is introduced to quantify the extent of mixing between the two materials. Dilution is often reported in welding metallurgy as a means of quantifying the amount of base metal incorporated into the melt pool in a non-autogenous weld [21,22]. By convention, the base material is treated as the diluent, such that 0 % dilution corresponds to pure weld filler material, and 100 % dilution corresponds to pure base material. If the two materials are of disparate concentration *(X)* in a particular element *(i)*, the dilution (D_i) in a weld may be calculated by

$$D_i = \frac{X_{i,\ Weld} - X_{i,\ Filler}}{X_{i,\ Base} - X_{i,\ Filler}} \quad (1)$$

2.1. Thermodynamic simulations

For simulations, intermediate compositions were calculated in increments of 10 % dilution, assuming the same D_i for every element in the system. As indicated in Fig. 1, each calculated composition was first assessed via the Scheil solidification and equilibrium modules in ThermoCalc software. For comparison, both the TCNI-11.0.1 database for Ni-alloys and the TCHEA-5.1 database for high entropy alloys were employed in the simulations. ThermoCalc's database documentation [23] was used to interpret the predicted phases in the results. Fig. 2 summarizes the simulated phase fractions for all prospective minor phases for both databases and both simulation modules. The major phase, constituting the remainder of the material up to a phase fraction of 1.0, always consisted of a disordered FCC solid solution matrix. Phase fractions are presented at the termination of the solidification sequence for the Scheil simulations, and at a temperature of 843 °C for the equilibrium simulations. 843 °C was selected because it is the final aging temperature in the industrially recommended heat treatment for Alloy 738LC [20]. As shown in Fig. 2, a total of eleven prospective minor phases are predicted to form in at least one of the simulation modules for at least one dilution level. Nine of these phases can be sub-categorized as disordered solid solutions, carbides, geometrically close-packed (GCP) ordered intermetallics, or topologically close-packed (TCP) ordered intermetallics.

Two disordered BCC solid solutions are predicted. One, labeled BCC in Fig. 2, is prevalent across many dilution levels in the Scheil module at phase fractions up to 0.01, and at dilution levels less than 50–60 % in the equilibrium data at phase fractions up to 0.06. The other, labeled BCC#2, is only predicted in very small phase fractions at high dilution levels in the Scheil module. A carbide phase with MC stoichiometry is predicted at every dilution level of 10 % or more in the Scheil data, and between dilution levels of 20–90 % in the equilibrium data. At the Alloy 738LC base material composition (100 % dilution), the equilibrium carbide at 843 °C is instead predicted to have $M_{23}C_6$ stoichiometry. The MC carbide phase fraction increases with dilution level and approaches 0.01 near the Alloy 738LC composition in both simulation modules, while the $M_{23}C_6$ phase fraction exceeds 0.02 in the condition for which it is predicted. In terms of performance, the prediction of carbide phases is benign, as carbides are found in most Ni-base superalloys and offer direct and indirect strengthening contributions [24]. The GCP phases include γ' and η, which are also generally neutral to beneficial microstructural constituents [24]. γ' is the main strengthening phase for Alloy 738LC and a range of precipitate-strengthened Ni-superalloys, and is critical in providing high-temperature strength [25]. η-phase, though typically not employed as a strengthening phase at service conditions, may assist in microstructural control during processing of certain

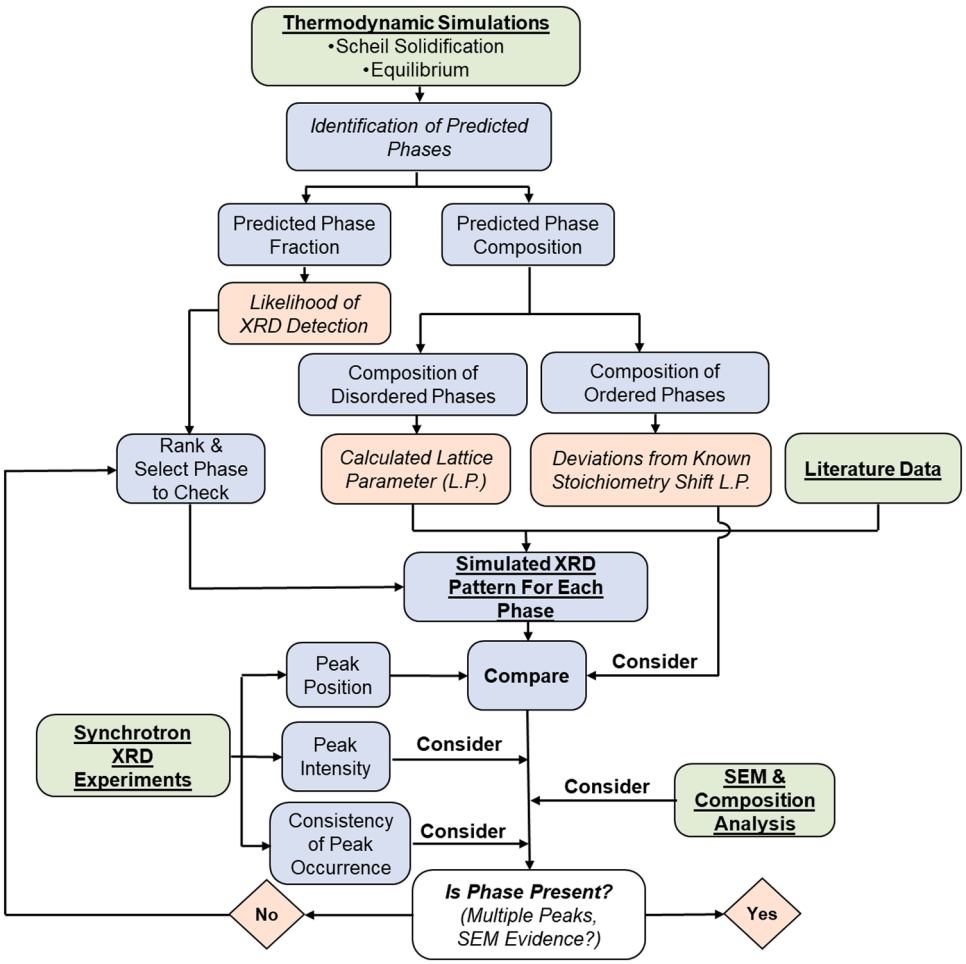

Fig. 1. Flow-chart describing the workflow combining simulated and experimental data to identify phases present in the mixed-CCA composition space investigated. Green boxes represent information input to the workflow, blue boxes represent intermediate analytical steps, and orange boxes represent information output from the preceding steps.

superalloys [24]. Fig. 2 shows that γ' is only predicted in equilibrium conditions, first appearing at a dilution level of 50 % and steadily increasing in abundance as dilution increases, reaching a phase fraction exceeding 0.45 in the Alloy 738LC composition. The η-phase only appears at dilution levels of 90–100 % in the non-equilibrium Scheil simulations. However, it is predicted to be the most abundant minor phase for these compositions in these simulations, with a phase fraction exceeding 0.05 for 100 % dilution in the HEA database prediction. The brittle TCP phases, which include σ, μ, and Laves phase, are always detrimental to performance [24,26,27]. Fig. 2 indicates that these phases are only predicted by the Scheil solidification simulations and not in equilibrium conditions. σ and μ are predicted by both databases when dilution exceeds 70 %, and Laves phase is predicted primarily by the Ni database when dilution is between 10 % and 50 %. The two additional phases predicted are δ and the Heusler phase. δ is commonly observed in certain superalloys and is often considered detrimental, as it causes depletion of strengthening precipitates, although some beneficial aspects are also noted [28]. The Heusler phase is occasionally discussed in both MPEA and Ni-alloy literature and reported to be brittle [29,30]. Fig. 2 illustrates that δ and the Heusler phase, as well as the BCC#2 solid solution, only appear intermittently and at very small predicted phase fractions in the simulation data. Therefore, δ, Heusler, and BCC#2 were disregarded in subsequent analysis.

Broadly, the simulated results from each of the two databases were similar, although comparing Fig. 2(a) and (b) shows that the HEA database consistently predicts higher phase fractions of minor phases across the compositions assessed by the Scheil module. The results from the HEA database were therefore considered a more conservative prediction of the minor phases that would need consideration in experimental data, and this database was used in subsequent analysis.

As indicated in Fig. 1, the simulated phase composition is another important output of the thermodynamic simulations, as it is critical to calculate the lattice parameter of disordered phases, and it assists in interpreting deviations from reported pure-phase lattice parameters for ordered phases. The composition data output from the HEA database for select prospective minor phases is provided in Fig. 3, with any elements whose concentration is below 1 at. % omitted. The phases shown are those predicted to exist at appreciable phase fractions across a broad range of dilution levels. Composition data from equilibrium simulations is reported at 843 °C. Composition data from Scheil simulations is averaged stepwise over the precipitation of the phase in the simulated solidification sequence, according to the equation:

$$X_{i,\,\phi} = \frac{1}{f_{\phi,\,N}} \sum_{j=1}^{N-1} \left(f_{\phi,\,(j+1)} - f_{\phi,j} \right) * \; X_{i,j} \tag{2}$$

where X is the concentration of any element i in phase ϕ, N represents the total number of simulation steps taken in the Scheil solidification sequence, j represents any given simulation step number, and f represents the fraction of phase ϕ at a given simulation step.

Fig. 3(a) shows that the prospective BCC phase is predicted to contain Ni, Mn, Al, Co, Cr, and Ti. For simplicity, only the equilibrium composition data are shown, but the Scheil module predicts similar

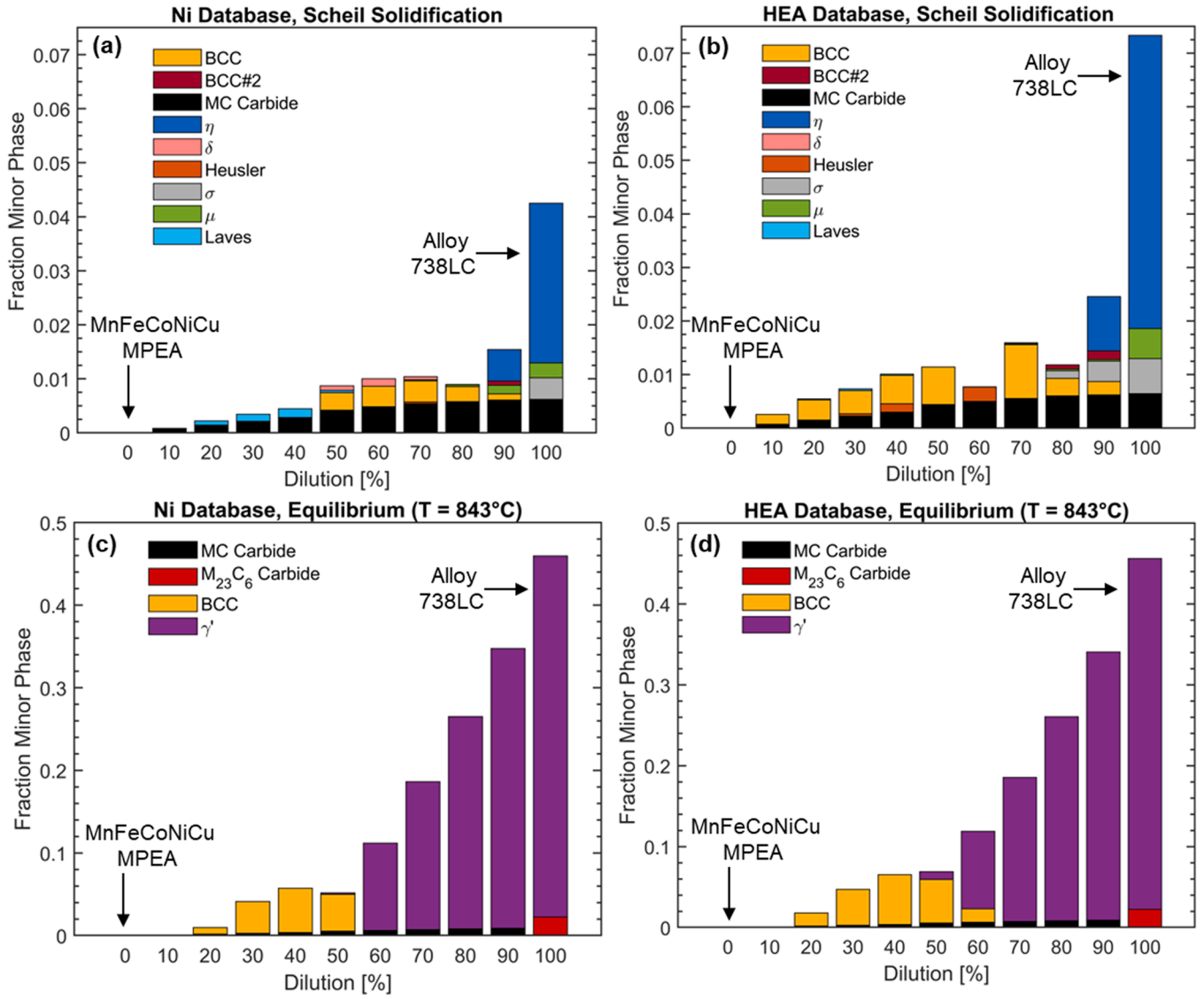

Fig. 2. Summary of phase fractions predicted by thermodynamic simulations for all phases except the disordered FCC solid solution matrix, which comprises the balance. (a, b) Scheil solidification module. (c, d) Equilibrium module at a temperature of 843 °C. (a, c) Using TCNI-11.0.1 database. (b, d) Using TCHEA-5.1 database.

trends in the composition data as dilution varies. Fig. 3(b) indicates that Ti and Nb are predicted to be the main metal atoms in the MC carbide phase, with minor concentrations of Ta and W. In Fig. 3(c), the predicted composition of γ' is consistent with its known stoichiometry of $Ni_3(Ti, Al)$, although γ' is predicted to dissolve increasing amounts of Mn, Co, and Ta as the dilution level decreases below 100 %, i.e., as MnFeCoNiCu MPEA is mixed with Alloy 738LC. Finally, Fig. 3(d) shows that σ is predicted to be rich in Cr, Co, Mo and Ni, while the constituents of the Laves phase are Ta, Co, Ni, Mn, and Cr.

As introduced in [18], a statistical hard-sphere approximation can be used in conjunction with reported atomic radii data [5] to calculate the lattice parameter of a disordered solid solution for any composition. The following equations are used for FCC and BCC structures, respectively:

$$a_{FCC} = \left(\frac{1}{\sqrt{2}}\right) \sum_{k=1}^{n^3} (X_{Ak} * X_{Bk} * X_{Ck}) * (r_{Ak} + 2r_{Bk} + r_{Ck}) \quad (3)$$

$$a_{BCC} = \left(\frac{1}{\sqrt{3}}\right) \sum_{k=1}^{n^3} (X_{Ak} * X_{Bk} * X_{Ck}) * (r_{Ak} + 2r_{Bk} + r_{Ck}) \quad (4)$$

where a is the lattice parameter, n is the number of elements in the system, k is a unique permutation of three elements A, B, and C in the system, which may include repeats, X is the concentration of an element in atomic fraction, and r is the reported atomic radius of an element. Note that the identities of A, B, and C change as the permutation index k varies from 1 to n^3. The calculated lattice parameter for the simulated compositions of the prospective BCC phase is included in Fig. 3(a). As indicated in Fig. 1, this model for estimating the lattice parameter of an unreported solid solution phase composition is assistive in assessing the presence of such a phase in XRD experiments.

2.2. Simulated X-Ray diffraction patterns for prospective phases

The composition information output from the thermodynamic simulations, such as that displayed in Fig. 3, was used to inform the input crystal structure used to simulate an XRD pattern for each prospective phase, building a system-specific diffraction library. The strategy for selecting the input crystal structure differed for disordered (solid-solution) and ordered (non-solid-solution) phases as shown in Fig. 1 and described in the following sections. Once an input structure was

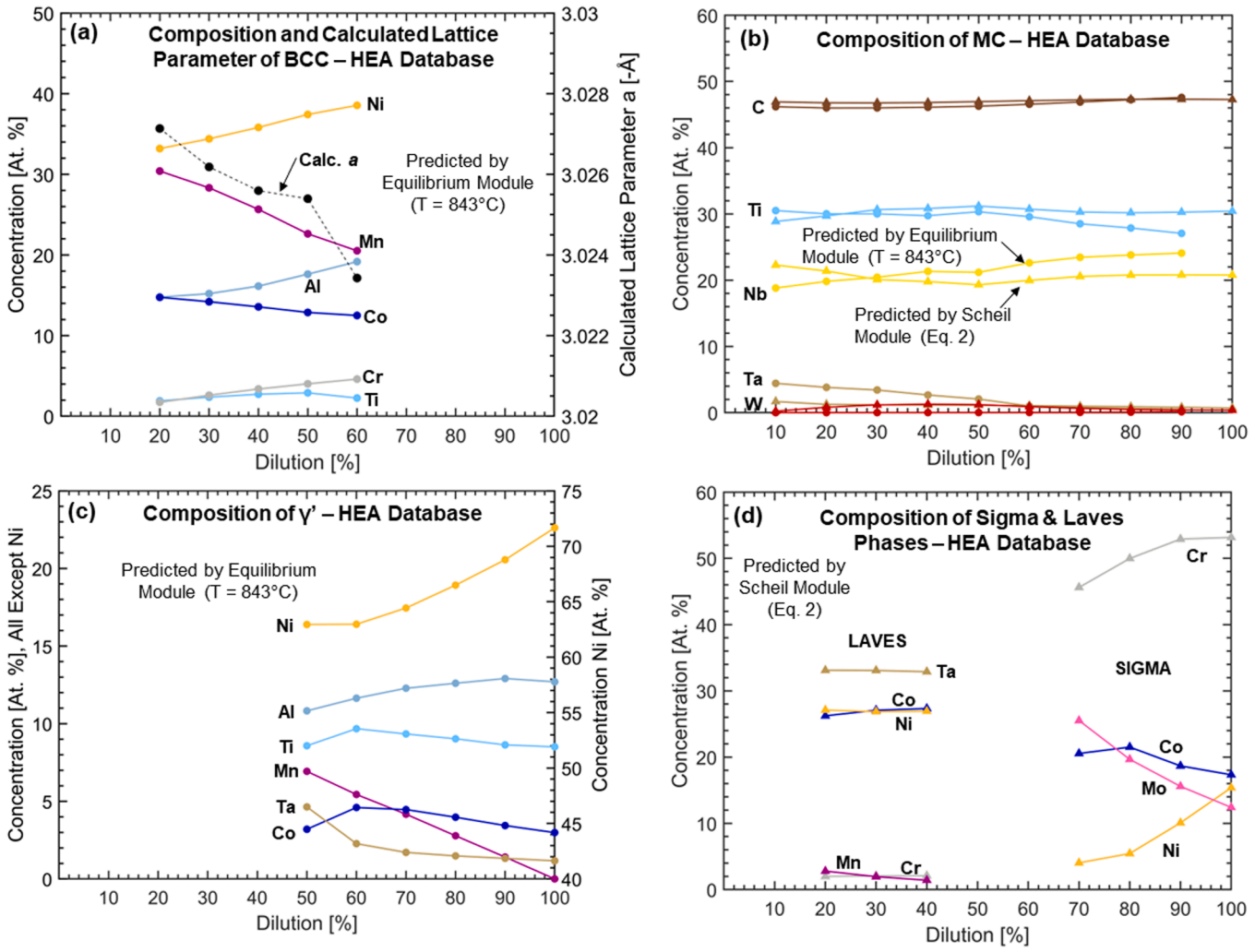

Fig. 3. Simulated composition data for select prospective phases in the MPEA/Alloy 738LC system. Circles represent data from the equilibrium module, and triangles represent data from the Scheil solidification module. (a) BCC solid solution with the lattice parameter *a* calculated via Eq. (4) included. (b) MC carbide. (c) γ'. (d) Sigma and Laves TCP phases.

selected, all pattern simulations were performed using GSAS-II software [31] with powder-pattern assumptions. The 2θ coordinate was converted to the wavelength-independent reciprocal lattice vector q, where $q = 2\pi/d$, with d representing the atomic interplanar spacing. Fig. 4 summarizes the input crystal structures and resultant simulated patterns.

2.2.1. *Disordered solid-solution phases*

As indicated in Fig. 1, because the compositions of the solid solution prospective phases are undocumented in the literature, the lattice parameter calculated via the simulated composition data and Eqs. (3) and (4) was essential to simulate their XRD patterns. Every solid solution composition across the range of dilution levels has a unique calculated lattice parameter, as demonstrated in Fig. 3(a), and the estimated peak positions for each composition vary correspondingly. Figs. 4(a) and (b) show renderings of example compositions of the FCC matrix and BCC prospective phases and the accompanying simulated patterns. Two unit-cells in each dimension are illustrated in the renderings, to demonstrate the disordered nature of the phases and more accurately depict the average composition, but a single unit cell with lattice parameter calculated via Eqs. (3) and (4) was used to simulate the patterns.

2.2.2. *Ordered intermetallic and carbide phases*

As shown in Fig. 1, existing literature data was primarily used to construct input structures for the ordered, non-solid-solution phases. Despite the variations in composition shown in Figs. 3 (b-d), crystal lattice parameters were fixed at reported literature values, but the predicted compositions guided structure selection and assisted in accounting for experimentally observed *d*-spacing discrepancies, as described in Section 4.3. For the γ' phase (Fig. 4c), the cubic ordered $L2_1$ Ni_3Al structure [32] was input, with the lattice parameter a adjusted to the reported value of 3.58857 Å in Alloy 738LC [33]. For the η phase (Fig. 4d), the hexagonal close-packed ordered $D0_{24}$ Ni_3Ti structure [34] was input, and lattice parameters were not adjusted from the reported values. It has been reported that η has very low solubility for elements other than Ni and Ti [24], so any substitutional uptake of extrinsic elements affecting the lattice parameters would be minimal. Based on the simulated composition of the MC carbide in Fig. 3(b), the TiC structure [32] was input for this phase, with the consideration that some deviation from the simulated peak positions (Fig. 4e) would be possible in experiments due to substitution of Nb, Ta, and W for Ti. Under similar logic, $Cr_{23}C_6$ [32] was selected as the representative structure for the $M_{23}C_6$ phase (Fig. 4f).

For the three TCP phases, simulated composition data heavily informed structure selection. Hall and Algie summarize the common, known binary σ-phase compositions and their ordering schemes [35]. Based on the simulation output in Fig. 3(d), the prospective σ-phase most closely resembles $Cr_{53}Co_{47}$, with significant substitution of Co by

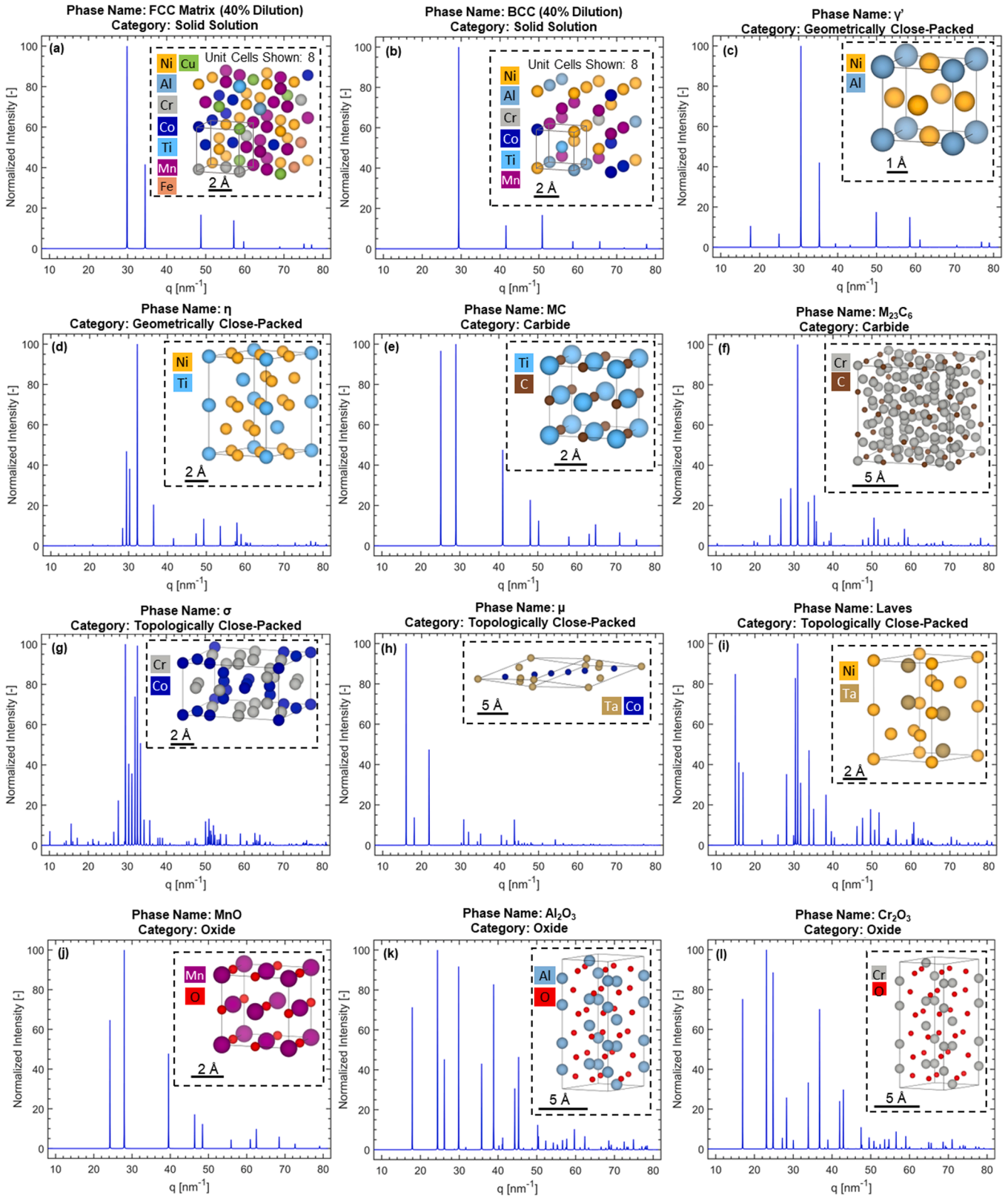

Fig. 4. The system-specific diffraction library. Shown are the crystal structures and simulated XRD patterns for (a-i) prospective phases output from the thermodynamic simulations, and (j-l) prospective oxide phases in the system. (a) FCC matrix. (b) BCC solid solution phase. (c) γ'. (d) η. (e) MC carbide. (f) $M_{23}C_6$ carbide. (g) σ. (h) μ. (i) Laves. (j) MnO. (k) Al_2O_3. (l) Cr_2O_3.

Ni and Mo. The input structure for σ (Fig. 4g) was therefore constructed based on the ordering scheme for $Cr_{53}Co_{47}$ [35], with lattice parameters taken from Wilson [27]. The μ-phase has stoichiometry A_6B_7 with the ordering scheme given by Sinha [26] and lattice parameters given by Wilson [27]. Simulated composition data provide a stoichiometry consistent with Ta, W, Nb, Mo, and Fe occupying "A" sites, and Co, Ni, and Cr occupying "B" sites in the prospective simulated μ-phase. To simplify the input structure (Fig. 4h), the stoichiometry was approximated as Ta_6Co_7. For the Laves phase, the predicted superlattice structure in ThermoCalc was C14, which corresponds to the $MgZn_2$ prototype with ordering scheme as described by Sinha [26]. Typical lattice parameters in a Ni-alloy environment are provided by Wilson [27]. The stoichiometry of the Laves phase is AB_2, and simulated composition data in Fig. 3(d) is consistent with Ta occupying "A" sites and Ni and Co occupying "B" sites along with minor concentrations of Mn and Cr. For the input structure (Fig 4i), the stoichiometry was simplified to $TaNi_2$. Table 1 summarizes the simulated phase structures and stoichiometric formulas.

2.2.3. Oxides

Although oxygen was not included in the thermodynamic simulations to avoid a confounding variable in the prediction of prospective phases, the cast MnFeCoNiCu-type MPEA was found to have sufficient oxygen content [36] that consideration of prospective oxide phases in the material system was required. Figs. 4(j-l) illustrate graphical renderings and simulated XRD patterns for three oxides likely to form in the material system – cubic MnO, hexagonal Al_2O_3, and hexagonal Cr_2O_3. Input structures for each of these phases were taken from [32] with the lattice parameters unaltered. In subsequent analysis, the simulated peak positions for the twelve prospective phases summarized in Fig. 4 served as a library specific to the MPEA/Alloy 738LC material system for the purpose of comparison with experimental data.

3. Experimental procedures

To experimentally validate the thermodynamic predictions of the constituent phases that form in the MnFeCoNiCu-type MPEA/Alloy 738LC material system, a layered sample was fabricated with laser-welding employed to mix the two materials to varying degrees and thus achieve variable levels of dilution according to Eq. (1). After the resultant, mixed compositions re-solidified, site-specific XRD was performed using a synchrotron x-ray beam, and the compositions were characterized further by scanning electron microscopy (SEM) and energy-dispersive spectroscopy (EDS). Essential aspects of the laser-mixing and synchrotron XRD experiment setups are illustrated schematically in Fig. 5 and described in the following sections.

Table 1
Summary of input parameters for simulated XRD patterns for each prospective phase.

Phase	Input Structure Formula	Space Group	Lattice Parameter (s)	References
FCC Matrix	Variable	$Fm\bar{3}m$ (#225)	Calculated	-
BCC	Variable	$Im\bar{3}m$ (#229)	Calculated	-
γ'	Ni_3Al	$Pm\bar{3}m$ (#221)	$a = 3.589$ Å	[32,33]
η	Ni_3Ti	$P6_3/mmc$ (#194)	$a = b = 5.096$ Å $c = 8.304$ Å	[24,34]
MC	TiC	$Fm\bar{3}m$ (#225)	$a = 4.336$ Å	[32]
$M_{23}C_6$	$Cr_{23}C_6$	$Fm\bar{3}m$ (#225)	$a = 10.552$ Å	[32]
σ	$Cr_{53}Co_{47}$	$P4_2/mnm$ (#136)	$a = b = 8.78$ Å $c = 4.54$ Å	[27,35]
μ	Ta_6Co_7	$R\bar{3}m$ (#166)	$a = b = 4.755$ Å $c = 2.583$ Å	[26,27]
Laves	$TaNi_2$	$P6_3/mmc$ (#194)	$a = b = 4.85$ Å $c = 7.93$ Å	[26,27]

3.1. Material preparation

The MPEA of approximate composition $Mn_{35}Fe_5Co_{20}Ni_{20}Cu_{20}$ was cast via button arc-melting from pieces of its pure constituent elements as described in [15]. Cast buttons were subsequently machined by milling to remove all visible surface oxide, although the oxygen content of the bulk filler remained above 1000 ppm [36], necessitating the consideration of oxide phases discussed in Section 2.2.3. Alloy 738LC was received in its as-cast state from an external supplier.

Both materials were subjected to a recrystallization treatment to reduce the grain size compared to the as-cast condition, to increase the diffracting grain population and allow for easier observation of XRD peaks caused by minor constituent phases. Epitaxial growth from the Alloy 738LC substrate in the solidifying pool made it particularly important to reduce the grain size in the substrate to achieve a sufficient diffracting grain population in the melt pool. The recrystallization treatment for the Alloy 738LC involved solutionizing at 1180 °C for 24 h, followed by water quenching and cold-rolling to 10 % reduction in thickness, and recrystallizing at 1180 °C for 15 min, followed by air cooling. The cast MnFeCoNiCu MPEA was rolled at 400 °C to 50 % reduction in thickness, and subsequently recrystallized at 850 °C for 2 h. These thermomechanical processing routes reduced the grain size from greater than 5 mm to 100 - 200 μm for Alloy 738LC, and from greater than 100 μm to 10 – 40 μm for the MPEA, determined using electron backscatter diffraction (EBSD).

Following the recrystallization treatments, each material was cut to the dimensions depicted in Fig. 5(a) using a slow-speed saw to accurately limit the specimen thickness to 0.5 mm. Limiting this dimension to 0.5 mm allowed the laser to melt the entire thickness, such that site-specific XRD data could be collected solely from fully melted material. After cutting, the Alloy 738LC pieces were heat-treated at 843 °C for 24 h to re-introduce γ' into the material, as recommended by [20]. Specimens were then assembled as shown in Fig. 5(a), using adhesive to affix a strip of MPEA atop the thin edge of the Alloy 738LC substrate piece.

3.2. Synchrotron XRD laser mixing experiments

Both laser-melting and synchrotron XRD data collection were performed at Beamline 1-ID-E of the Advanced Photon Source, Argonne National Laboratory. Laser-melting with an IPG YLR-500-AC-Y11 ytterbium fiber laser was carried out in an argon environment to melt the two materials together, as shown in Figs. 5(a-b). The laser traversed 2 mm and the laser scan speed was fixed at 10 mm/s for all experiments, but the laser power was varied from 160 W to 220 W to achieve varying degrees of material mixing. A laser was also used to melt solely the Alloy 738LC, with no MPEA mixed in, for comparison. The constituent phases and solidification behavior of the MPEA alone were characterized in previous work [18].

After laser melting, site-specific XRD patterns were collected from the melt pool and adjacent substrate material, as shown in Fig. 5(b-c). For comparison, patterns were also collected from un-melted MPEA and Alloy 738LC materials prior to laser melting. For pattern collection, a monochromatic beam with energy of 61.332 keV was directed in transmission through the samples, with incident beam dimensions of 100 μm horizontally by 50 μm vertically defined by two sets of slits. A Pilatus3 X CdTe 2 M hybrid photon counting detector with a sample-to-detector distance of 740 mm was used to collect patterns. The laser welds were translated horizontally and vertically in increments equal to the dimensions of the incident beam, creating a continuous spatial map of XRD patterns that extended 1 mm laterally and 2 mm below the original top surface of the specimen, as detailed in Fig. 5(b). Patterns were integrated using fit2D software and averaged over each row

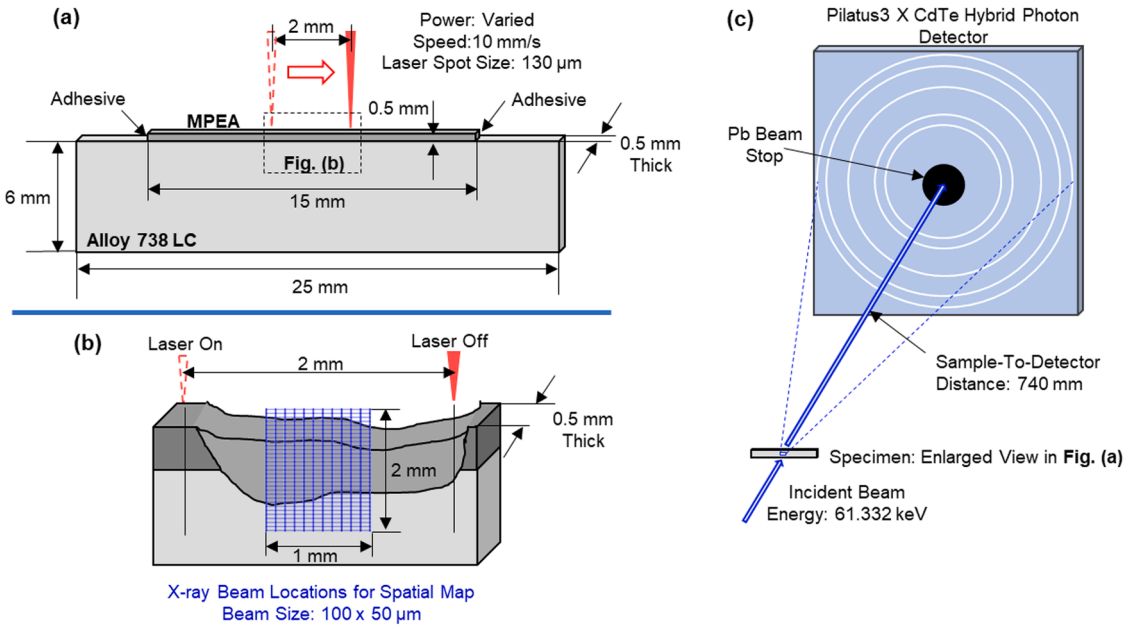

Fig. 5. Schematic illustrations of the experiment setup for synchrotron XRD to assess the constituent phases across a range of CCA compositions. (a) Thin-walled specimen geometry including Alloy 738LC substrate and a strip of MnFeCoNiCu-type MPEA on top. (b) Close-up view of specimen after mixing the two alloys by laser welding and the corresponding incident x-ray beam locations for spatial mapping of diffraction patterns. (c) Macroscopic view of the far-field diffraction detection setup.

indicated in Fig. 5(b) to achieve a better powder average diffraction pattern than using an individual frame. Detectable peaks of any intensity were fit with a Pearson VII function [37], whose center was taken as the peak position and height was taken as the peak intensity. Pearson VII was selected over the conventional pseudo-Voigt function [38] because it proved more robust at programmatically fitting low-intensity peaks, and peak shape was not an important consideration in this analysis.

3.3. Scanning electron microscopy characterization

Following the laser-mixing experiments and characterization by synchrotron XRD, samples were prepared for microscopy by standard metallographic polishing with a final step of 0.05 μm colloidal silica on a vibratory polisher. No additional chemical etching was performed following vibratory polishing, as the colloidal silica polish offered sufficient imaging contrast in scanning electron micrographs. Subsequently, electron microscopy and EDS characterizations were performed using a Tescan S8252G SEM. Imaging was performed using an accelerating voltage of either 2 kV or 5 kV, and a beam current of either 100 pA or 300 pA. EDS was performed using an accelerating voltage of 20 kV and a beam current of 10 nA. Low-magnification EDS line-scans were performed across the weld pool/base material interface to assess the bulk composition of the melt pool and calculate the dilution achieved in each laser-mixed sample via Eq. (1). Higher magnification EDS maps were collected to identify the composition of particles in the microstructure and corroborate the identification of prospective phases made by analysis of the synchrotron XRD data. EDS data was quantified using the ZAF correction method. If particles were too small to be assessed by EDS-mapping, SEM images were used to corroborate the phase identification.

4. Results and discussion

4.1. Experimental dilution levels

For the sake of comparing to the simulated data in Fig. 2, the dilution level achieved in each laser-mixing experiment was determined by assessing the bulk composition of each melt pool. Fig. 6 shows an

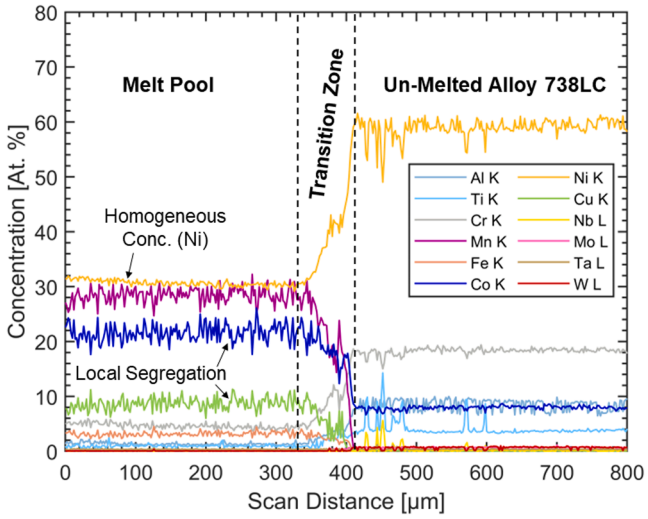

Fig. 6. Example of composition data collected via an EDS line scan to determine D_{Ni} level; laser power 180 W.

example of composition data from an EDS line scan taken across the interface between the melt pool and the un-melted Alloy 738LC for the weld performed using a power of 180 W. The bulk composition of each melt pool was fairly homogeneous, as confirmed by EDS mapping on large regions, except for sparse convection eddies near the bottom of the melt pool, which were avoided when taking line scans. Within the melt pool, dendritic/interdendritic segregation [18] resulted in local fluctuations in the concentration of Cr, Mn, Fe, Co, and Cu, as indicated in Fig. 6. Ni, which displays little tendency for segregation in the system [18], consistently demonstrated the greatest homogeneity in concentration throughout each melt pool. For this reason, Ni was selected as the basis element for calculating the dilution level via Eq. (1), and subsequent values of dilution are reported as D_{Ni}. Measured D_{Ni} levels ranged from 8.1 % at a laser power of 160 W to 55.3 % at a laser power of 220 W. Dilution levels greater than 55.3 % were difficult to achieve because

increasing laser power above 220 W led to a high degree of material ablation. However, the specimen where Alloy 738LC was melted alone without mixing any MnFeCoNiCu-type MPEA represented a D_{Ni} value of 100 %.

4.2. Peak indexing

Fig. 7 shows representative synchrotron XRD patterns from the two, separate un-melted (UM) materials, and from fully-melted (FM) samples spanning the full range of D_{Ni} values achieved experimentally. As clearly indicated in the patterns, the peaks corresponding to the major,

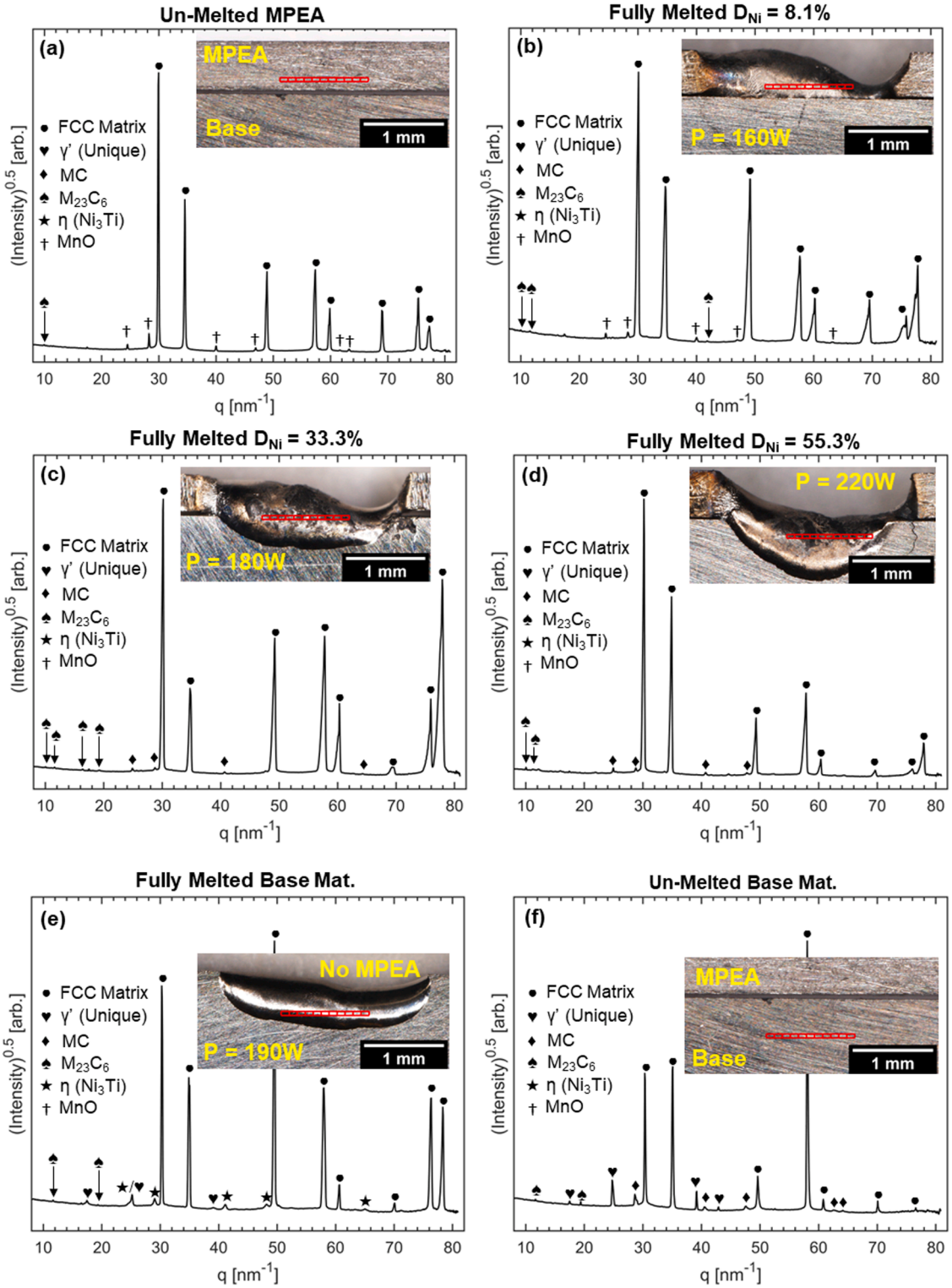

Fig. 7. Representative XRD patterns averaged over the locations indicated by the red rectangles in the inset macroscopic images. (a) Un-melted MnFeCoNiCu MPEA. (b-d) Fully melted zones of laser welds with a measured D_{Ni} of (b) 8.1 %, (c) 33.3 %, (d) 55.3 %. (e) Fully melted Alloy 738 LC alone (D_{Ni} = 100 %). (f) Un-melted Alloy 738LC.

disordered FCC solid solution phase were easily identifiable due to their high relative intensity and positions approximately matching the simulated data in Fig. 4(a).

As outlined conceptually in Fig. 1, the remainder of the complete set of experimental XRD peaks was systematically assigned to minor constituent phases via an iterative process. First, the likelihood of a given phase being present and detectable by XRD at the experimentally measured dilution/melting condition was assessed based on the simulated phase fraction data in Fig. 2. For FM material, the constituent phases were expected to match Scheil simulation data more closely than equilibrium, although it was necessary to consider evolution toward equilibrium that occurred as the material cooled. For the individual UM materials, it was expected that the material would closely match equilibrium conditions at 843 °C, as the final steps of the preparation routes described in Section 3.1 were heat treatments at 850 °C for the MPEA and 843 °C for Alloy 738LC.

If a phase was determined from Fig. 2 to be probable, the fitted experimental peak positions were directly compared to the simulated peak positions for that phase in Fig. 4. Although peak intensity was qualitatively considered, because of solidification texture and large grain size, peak position was the most critical attribute in assigning experimental peaks to a constituent phase. However, the experimental peak positions often deviated appreciably from simulations because of lattice parameter shift due to element substitution, which is predicted for certain example phases by the composition data in Fig. 3. To systematically account for this deviation, it was important to consider consistency of peak position among individual XRD patterns, both for a single dilution level and among all the dilution levels examined. To illustrate how this consistency of peak position was incorporated in phase identification, Fig. 8 shows a binned peak-frequency diagram for selected regions of the XRD spectrum. The color bar represents the number out of ten assessed patterns for a given dilution level in which a peak was positioned within a bin of size 0.025 nm^{-1} in q space. Peaks with an absolute intensity of less than 0.001 are excluded; for comparison, the absolute intensity values of major-phase peaks usually fell between 10 and 100. Note that the color bar in Fig. 8 does not reflect the

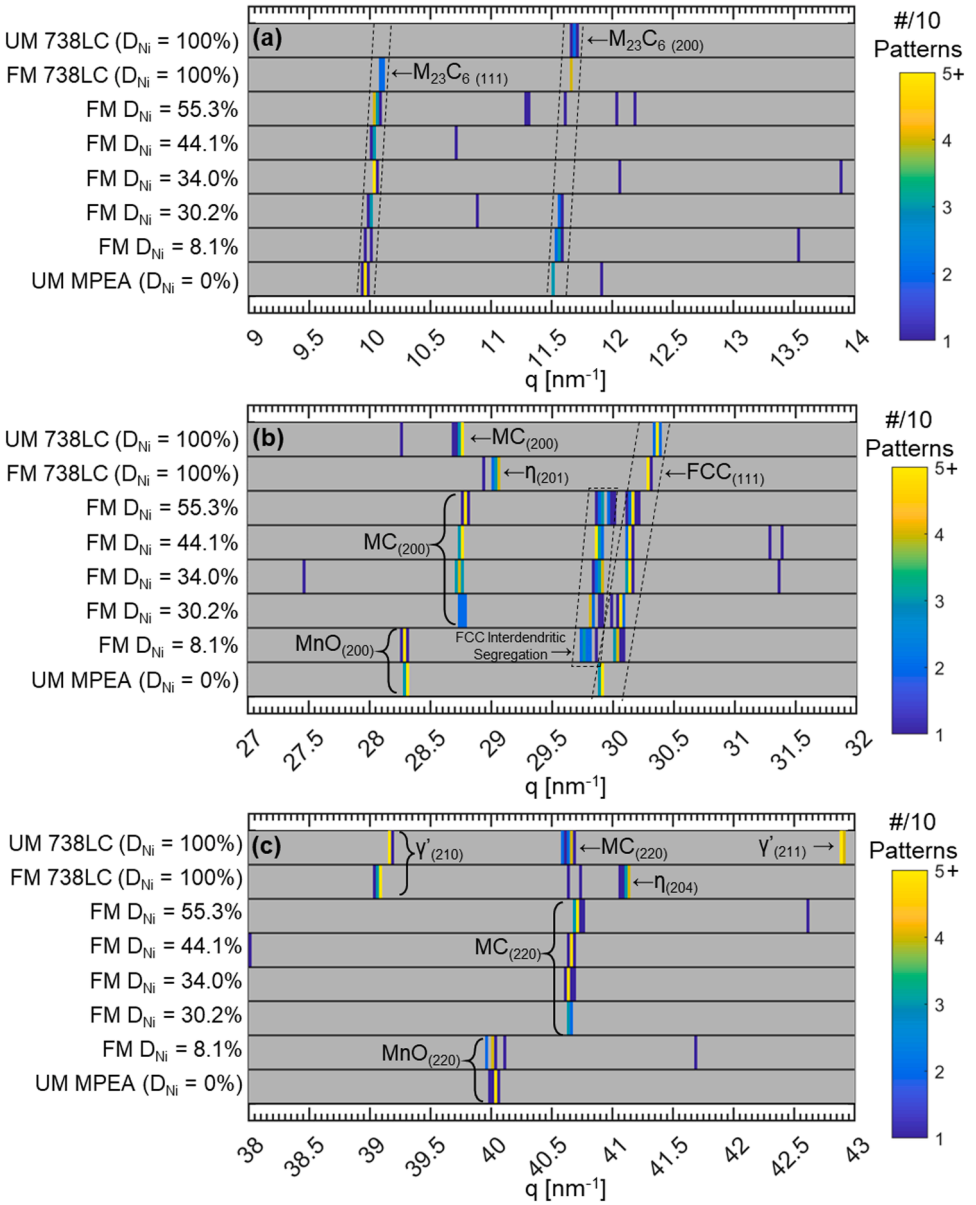

Fig. 8. Statistical peak-frequency diagrams for select regions of the XRD spectrum displaying the number out of ten patterns for which a peak of absolute intensity greater than 0.001 was centered within a bin of 0.025 nm^{-1} in q-space. (a) q = 9 – 14 nm^{-1}. (b) q = 27 – 32 nm^{-1}. (c) q = 38 – 43 nm^{-1}. FM = fully melted, UM = un-melted.

value of peak intensity, but relative intensities of peaks corresponding to each phase can be gleaned from the representative patterns in Fig. 7.

Fig. 8(a), showing $q = 9 – 14$ nm^{-1}, clearly indicates the presence of sets of peaks spanning the full range of experimental D_{Ni} values, even though the intensity of these peaks is so low that they are almost indiscernible in Fig. 7. The peak-frequency diagram clearly delineates consistently occurring low-intensity peaks from other, randomly-occurring low-intensity peaks that are likely experimental artifacts, i.e., the unlabeled stray lines in the figure. Trends in peak position as a function of D_{Ni} are clearly observable for the peaks in Fig. 8(a), which are discussed in Section 4.3. Additionally, Fig. 8(b) and (c) illustrate regions of q-space that show the distinction between nearly overlapping peaks more clearly than Fig. 7 does. This distinction is critical when correlating XRD peaks with features observed in secondary electron micrographs and corresponding EDS data spanning the range of dilution levels, such as the images shown in Figs. 9 and 10. As indicated by Fig. 1, SEM and EDS analysis constituted the final information input to the phase identification workflow to ensure XRD peaks were assigned to correct microconstituents. If multiple diffraction peaks with reasonably small deviation in position from simulated data for a given phase were presented alongside identifiable, correlating features in SEM and EDS analysis, the phase was determined to be present, and the corresponding peaks assigned. If not, the phase was determined to be absent and the next-most-probable phase assessed. Using this strategy, 96.8 % of fitted peaks with an absolute intensity greater than 0.01 and 99.0 % of those with an absolute intensity greater than 0.1 were assigned to a phase.

4.3. Experimentally presented minor phases

Fig. 7(a) and (b) show a series of MnO peaks for UM $D_{Ni} = 0$ % and FM $D_{Ni} = 8.1$ %, and Figs. 9(a) and 10(a) confirm the presence of MnO particles exceeding 10 μm in length for FM $D_{Ni} = 8.1$ %. At higher dilution levels, no MnO is identifiably present. This finding indicates that MnO particles, present in the UM MPEA due to insufficient environmental control during arc-casting [36], remained present in the relatively low heat-input laser weld when $D_{Ni} = 8.1$ %, but were fully re-dissolved into the matrix at higher weld heat-inputs and did not precipitate during cooling.

Figs. 7 and 8 indicate peaks consistent with the presence of the MC carbide phase for all FM $D_{Ni} \geq 30.2$ %, as well as UM $D_{Ni} = 100$ % (base Alloy 738LC). As an example, Figs. 9(b) and 10(b) demonstrate the presence of Ti-rich particles on the order of 1 μm in diameter when $D_{Ni} = 55.3$ %, which the composition data in Fig. 3(b) indicate correspond to the MC carbide phase. Figs. 9(d) and 10(d) clearly illustrate larger MC particles in the UM $D_{Ni} = 100$ %. As illustrated by Fig. 8(b) and (c), the MC diffraction signal is least consistent for FM $D_{Ni} = 100$ %, and no correlating features are observable for this material condition in Fig. 9 (c) and 10(c).

Although Fig. 7 indicates that the diffraction signal is of very low intensity, Fig. 8(a) clearly shows the consistent presence of low-temperature $M_{23}C_6$ carbides in every dilution level and melting condition. This finding is evidence that evolution toward equilibrium occurred as each laser-weld cooled. The $M_{23}C_6$ carbides in UM $D_{Ni} = 0$ % indicate that carbon is present in the as-cast MPEA, although this material is nominally carbon-free. However, the absence of MC carbide below $D_{Ni} = 30.2$ % indicates that a critical level of strong MC-carbide formers (primarily Ti) must be introduced to the MnFeCoNiCu-type MPEA before the MC phase is precipitated under laser-melting conditions.

As illustrated by Fig. 8(b) and (c), there is a consistent set of peaks unique to the FM $D_{Ni} = 100$ % material. Given the high fraction of η-phase predicted for this material in Fig. 2(b) and the approximate match to η peak positions in Fig. 4(d), these peaks were assigned to η. The correlating features present in Fig. 9(c), showing FM $D_{Ni} = 100$ %, are too small to resolve compositional enrichment with EDS in an SEM. However, these features lie along the Ti-rich segregation identified in Fig 10(c), which is consistent with the Ni_3Ti η-phase stoichiometry. Additionally, the near absence of MC carbide in this condition further indicates the presence of η, which would bind Ti in the system, limiting its availability to form carbides.

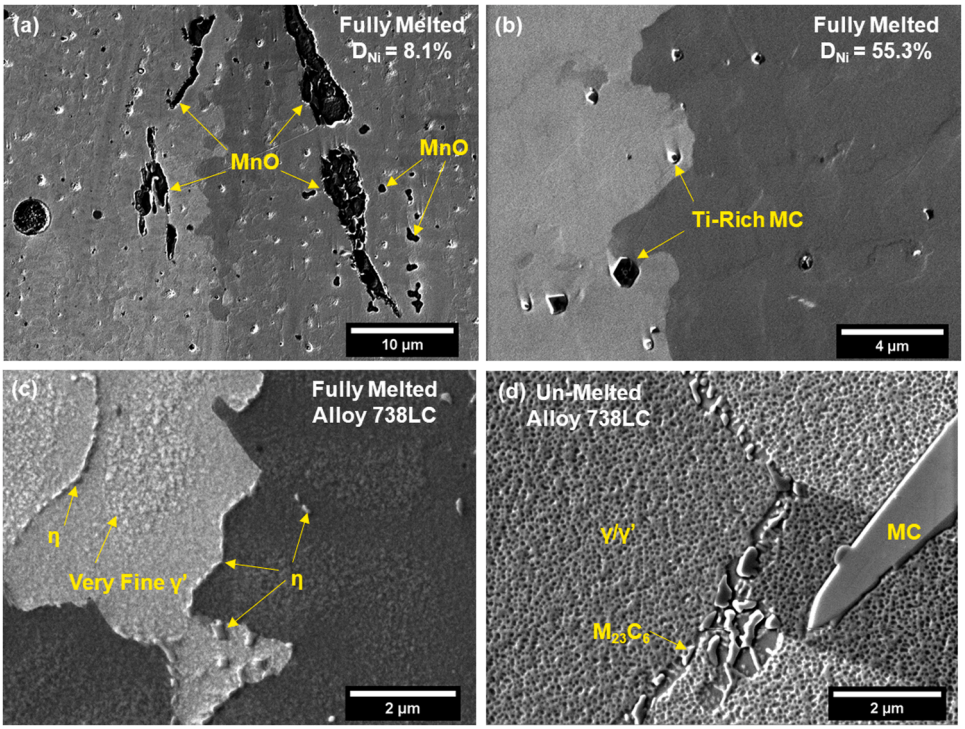

Fig. 9. Secondary electron images of each phase detected in the synchrotron XRD data, in selected specimens. (a) MnO in the FM $D_{Ni} = 8.1$ % condition. (b) MC carbides in the FM $D_{Ni} = 55.3$ % condition. (c) η and fine γ' in the FM Alloy 738LC base material. (d) Intragranular MC carbide and grain-boundary $M_{23}C_6$ carbides in the precipitate-hardened γ/γ' matrix of the UM Alloy 738LC base material.

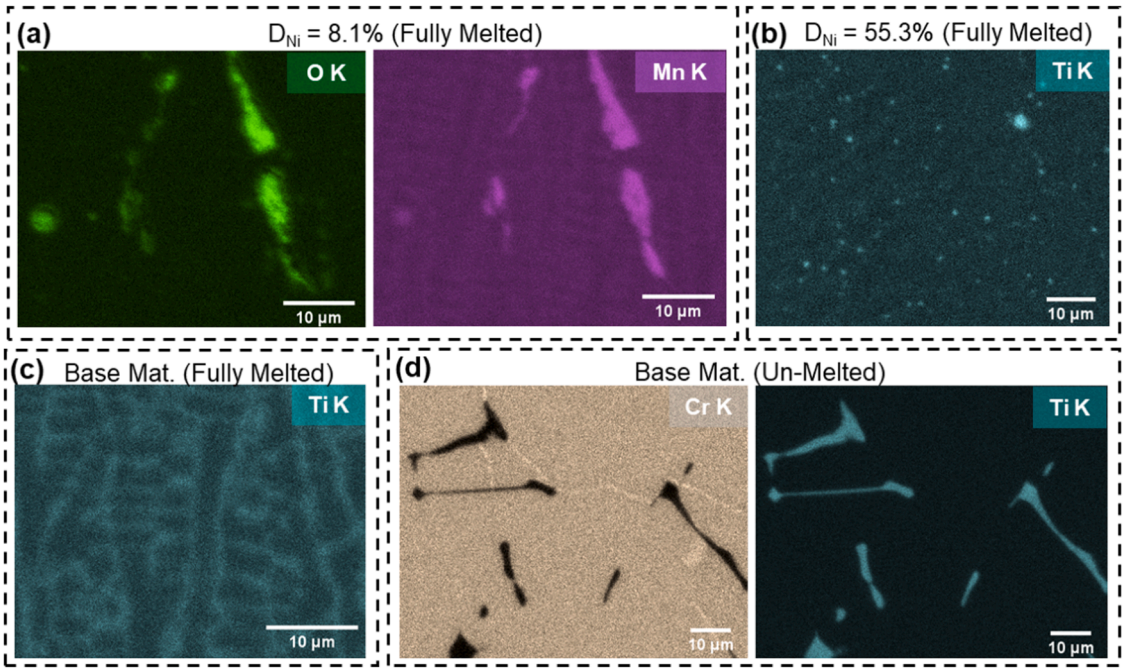

Fig. 10. EDS data corresponding to the specimens in Fig. (9). (a) MnO in the FM $D_{Ni} = 8.1$ % condition. (b) Ti-rich MC particles in the FM $D_{Ni} = 55.3$ % condition. (c) Ti-segregation in the FM Alloy 738 LC base material, corresponding to the locations of the η-phase. (d) Intragranular Ti-rich MC carbide and grain-boundary Cr-rich $M_{23}C_6$ carbides in the UM Alloy 738LC base material.

Figs. 7 and 8 show that the diffraction signal for γ' is present for both UM $D_{Ni} = 100$ %, and FM $D_{Ni} = 100$ %, although it is weaker for the fully melted material. Fig. 9(d) clearly shows γ' precipitates in the un-melted condition, while the fully melted condition in Fig. 9(c) presents very fine precipitates far away from the proposed η-phase, which are likely γ'. The detection of any γ' in the fully-melted condition is noteworthy, as γ' is not present in the Scheil simulations for this material (Fig. 2b), so this indicates some evolution toward equilibrium during specimen cooling. γ' is not detected at any experimental dilution level below 100 %. This agrees with the equilibrium simulation data in Fig. 2(c-d), since the highest experimentally achieved dilution for mixed material was 55.3 %, and the simulations indicate this dilution level is approximately the threshold at which appreciable γ' precipitation begins.

Together, six out of the twelve prospective phases from Fig. 4 were determined to be present in at least one experimental condition, including the major FCC solid solution phase and five minor phases. Fig. 11 summarizes the distribution of *d*-spacing determined from peak position encountered for each of the minor phases detected in each material, relative to the *d*-spacing of the simulated "pure" phase diffraction line in Fig. 4. Since the deviation in *d*-spacing is given as a relative percentage, and not in absolute terms, all peaks for a given phase are consolidated in the distribution. In Fig. 11, the absence of a box-and-whisker dataset indicates that the phase was not detected at the corresponding experimental condition on the plot's horizontal axis.

Fig. 11(a) shows that when γ' was detected, its *d*-spacings were highly consistent with the literature report for γ' in Alloy 738LC [33], with a median deviation of −0.0074 % in the un-melted condition and +0.18 % for the fully melted condition along with narrow statistical distributions. The positive deviation in the fully melted condition is attributable to tensile residual stresses imparted by laser-melting. Fig. 11(b) illustrates that the detected MnO displayed consistently smaller *d*-spacings than predicted for its pure manifestation [32], with a median deviation of −1.25 % for the un-melted $D_{Ni} = 0$ % and a median deviation of −1.20 % for fully melted $D_{Ni} = 8.1$ %. These negative deviations are attributable to substitution of Mn in the oxide phase by Fe, Co, Ni, and Cu – the other MPEA constituents – all of which have a smaller atomic radius than Mn [5]. Compared to the oxide, the η-phase has a smaller absolute value of median deviation of +0.45 %, but with a wider statistical distribution. This wide distribution may be due to the hexagonal structure of η, as any substitution may affect the c/a ratio, causing the *d*-spacing to expand in certain crystallographic directions and contract in others. In Fig. 11(c), the MC carbide phase displays consistent positive deviations from pure TiC [32] across all dilution levels in which the phase is presented, with median deviations ranging from +0.71 % to +0.86 %. These positive deviations are attributable to substitution of Ti by the other strong carbide formers in the system, Nb, Ta, and W, as predicted by Fig. 3(b). This example demonstrates how simulated composition data inform the analysis of experimental XRD, as indicated in Fig. 1.

Of all the minor phases, the $M_{23}C_6$ carbide displays by far the greatest deviations from its reference phase, $Cr_{23}C_6$ [32], with median deviations as high as +3.44 % in the un-melted $D_{Ni} = 0$ % material, as indicated by Fig. 11(d). As illustrated by the angled dashed lines in Fig. 8 (a), peak position for $M_{23}C_6$ is a function of dilution level, which is also reflected by the general decrease in *d*-spacing as dilution level increases in Fig. 11(d). Mn substitution for Cr is thought to heavily influence the lattice parameter of $M_{23}C_6$ as the bulk material composition changes. Moreover, the un-melted $D_{Ni} = 0$ % MPEA material is Cr-free, and the primary metallic species in $M_{23}C_6$ at this composition is predicted to be Mn. Mn has both the highest concentration in the MPEA and a greater affinity for carbon than other constituent elements like Fe, Co, and Ni [39]. The greater atomic radius of Mn relative to Cr contributes to the +3.44 % deviation when D_{Ni} is low and Mn substitution is likely, but it does not explain why the carbides in the Mn-free $D_{Ni} = 100$ % composition still display approximately +2 % deviation from $Cr_{23}C_6$. Given that the $M_{23}C_6$ phase has high solubility for a variety of metallic elements [40], other substitution is likely a factor, but further study is necessary to ascertain this.

4.4. Major FCC solid solution

The separate groupings of major phase (FCC solid solution) peaks in Fig. 8(b) illustrate that for any fully melted mixed material, each major-phase FCC peak was usually best fit using two separate Pearson VII

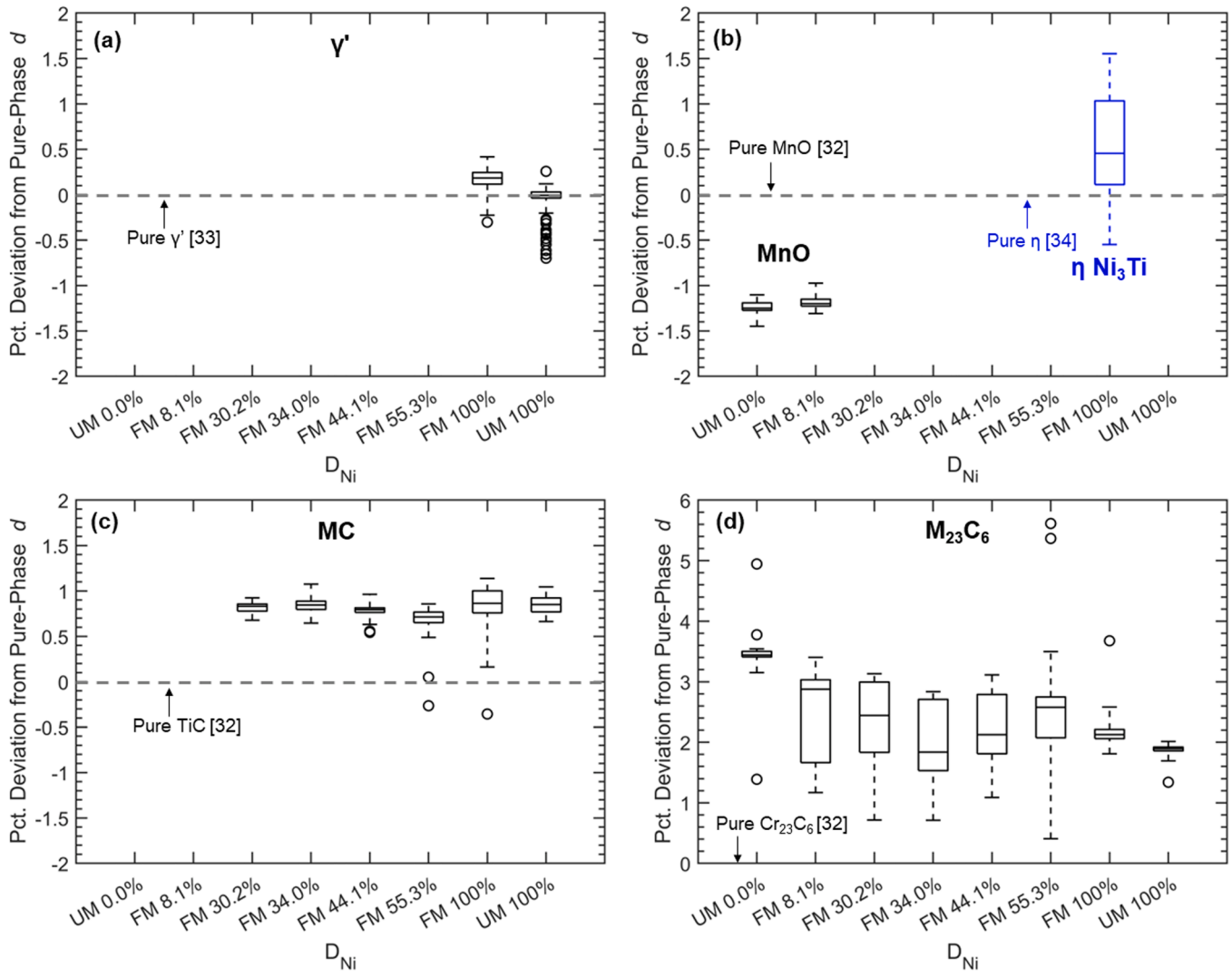

Fig. 11. Distribution of experimentally presented deviation in interplanar spacing relative to pure phase reference values, for all minor phases detected in the MPEA/Alloy738LC material system. (a) γ', (b) MnO and η-phase, (c) MC carbide, and (d) $M_{23}C_6$ carbide. Datapoints greater than three interquartile ranges deviant from the median are shown as outliers.

functions to accommodate peak asymmetry. This asymmetry is most visible in high-index major-phase peaks such as those in the right-hand portion of Fig. 7(b), and it is caused by dendritic/interdendritic segregation of compositions with disparate lattice parameters, described in detail in [18]. The interdendritic segregation corresponds to a lower-intensity shoulder peak that appears on the left-hand side of the main peak; the corresponding fitted peak centers are labeled in the frequency diagram in Fig. 8(b).

For the FCC matrix, Fig. 12 compares the experimentally observed lattice parameters with those calculated via Eq. (3) for the simulated matrix compositions in both equilibrium and Scheil conditions. Simulated equilibrium compositions are those at 843 °C, and simulated Scheil compositions are those calculated via Eq. (2). For experimental conditions in which an interdendritic segregation was observed (see Fig. 8b), the lattice parameters shown are averages of the main dendrite peak and interdendritic shoulder peaks, weighted according to peak intensity. Fig. 12 shows that all three datasets have downward trends with increasing dilution level. Of the two simulated datasets, the equilibrium data has a steeper downward trend in lattice parameter because γ' precipitation at high dilution levels (Fig. 2(c) and 2(d)) depletes the FCC matrix of Al and Ti, elements with relatively large atomic radii [5]. While the constituent phases present indicated that experimental conditions following solidification and cooling lay between pure Scheil and pure equilibrium, the experimental dataset in Fig. 12 more closely matches the behavior of the Scheil simulation, indicating that the Scheil model is a better predictor of matrix composition in the resultant laser weld.

Furthermore, the experimental dataset in Fig. 12 never deviates from the calculated lattice parameter for the Scheil-predicted compositions by more than 0.04 Å in either direction. At a dilution level of 100 %, the experimental lattice parameter is 3.592 Å, the literature-reported lattice parameter is 3.586 Å [33], and the lattice parameter predicted by Eq. (3) and Scheil composition data is 3.582 Å. Considering that factors other than composition that affect lattice parameter, such as residual stresses imparted by laser welding, are ignored in this analysis, this agreement is reasonable. A more detailed assessment incorporating estimated residual stresses in the laser welds could offer insights pertaining to the discrepancy in slope between the experimental and calculated datasets. Additionally, the analysis does not consider experimental deviations from uniform dilution in every element, e.g., excess losses of volatile elements such as Mn during laser melting, which may also affect the slope of the experimental dataset in Fig. 12. Overall, the agreement in trend and the approximate agreement in values across a range of alloy compositions validates the use of the statistical hard-sphere model in Eqs. (3) and 4 as a simple method to rapidly estimate the lattice parameter of an unknown, disordered solid solution.

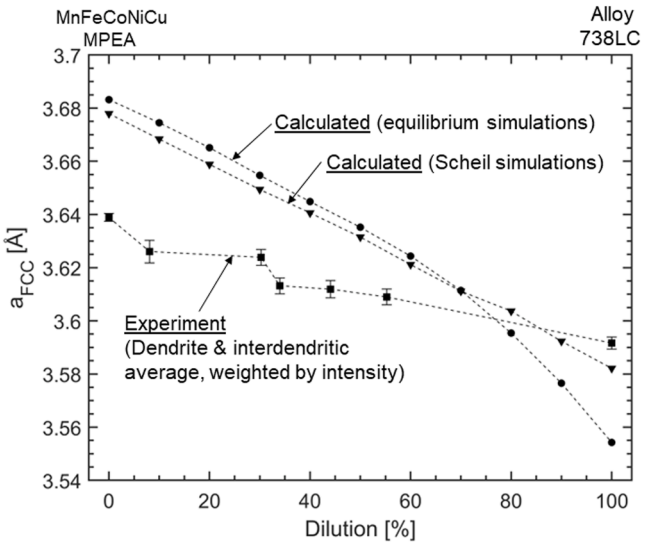

Fig. 12. Comparison of experimental and calculated lattice parameters of the FCC matrix as a function of dilution level. Calculated lattice parameters were found by employing Eq. (3) on composition data from equilibrium and Scheil simulations.

4.5. Absent phases

Generally, fewer phases were experimentally present than predicted by the simulated dataset in Fig. 2. None of the three TCP phases was detectable by XRD, and no experimental evidence of the BCC solid solution predicted to exist across many dilution levels in Fig. 2 was found. The TCP phases are all predicted in the Scheil solidification module, and their absence is therefore not attributable to insufficient evolution toward equilibrium. Instead, the phases are either present in such a low volume fraction as to be undetectable by XRD, or their fraction may be over-predicted by the simulation module. Considering the high successful peak-assignment rate of 99.0 % for peaks within three orders of magnitude of the maximum intensity, it can also be concluded that all present phases were accounted for by the system-specific diffraction library in Fig. 4; no unexpected phases were present. This finding is important in validating the construction of a simulated diffraction library to assist with phase identification for a novel material system such as that explored in this work.

5. Conclusions

1 For a mixed-CCA composition space transiting from a MnFeCoNiCu-type MPEA to the Ni-base Alloy 738LC, thermodynamic simulation data using ThermoCalc's TCNI 11.0.1 and TCHEA 5.1 databases guided the creation of a system-specific diffraction library that consisted of twelve prospective phases, including three oxides found in prior study.

2 Considering consistency of peak position, the statistical distribution of *d*-spacing, and correlating features in SEM data as guiding information, 99.0 % of peaks within three orders of magnitude of the maximum intensity were assigned to phases in the system-specific library. Deviations from literature *d*-spacings are largely attributable to element substitution in the complex system, validating the peak indexing.

3 Approximate agreement between calculated and experimental lattice parameters for the disordered FCC solid solution matrix phase validates the use of the statistical hard-sphere atomic model to rapidly estimate the lattice parameter and simulate an XRD pattern for disordered solid solutions in CCA systems.

4 Six of the twelve prospective phases were found to be experimentally present at some point in the system composition space including an FCC matrix, ordered cubic γ', ordered hexagonal η, an MC carbide, an $M_{23}C_6$ carbide, and manganese oxide. Notably, the three detrimental TCP phases and the BCC solid solution were absent. No unexpected phases were present in the experimental data, validating the use of thermodynamic simulations to construct a comprehensive diffraction library of prospective phases for the material system assessed.

Declaration of Competing Interest

The authors declare that they have no known competing financial interests or personal relationships that could have appeared to influence the work reported in this paper.

Acknowledgments

This research is supported by the National Science Foundation with Award No. 1847630. This research used resources of the Advanced Photon Source, a U.S Department of Energy (DOE) Office of Science User Facility operated for the DOE Office of Science by Argonne National Laboratory under Contract No. DE-AC02-06CH11357. Data was collected at Beamline 1-ID-E. Support from beamline staff was greatly appreciated. Use of the Tescan S8252G SEM was supported by the National Science Foundation Division of Materials Research Award No. 1828454. The authors would like to thank PCC-Structurals, Inc. for donating the Alloy 738LC material used in this study. Aric Adamson is acknowledged for his assistance in sample preparation.

References

[1] J.W. Yeh, S.K. Chen, S.J. Lin, J.Y. Gan, T.S. Chin, T.T. Shun, C.H. Tsau, S.Y. Chang, Nanostructured high-entropy alloys with multiple principal elements: novel alloy design concepts and outcomes, Adv. Eng. Mater. 6 (5) (2004) 299–303.
[2] B. Cantor, I. Chang, P. Knight, A. Vincent, Microstructural development in equiatomic multicomponent alloys, Mater. Sci. Eng. A 375 (2004) 213–218.
[3] F. Otto, Y. Yang, H. Bei, E.P. George, Relative effects of enthalpy and entropy on the phase stability of equiatomic high-entropy alloys, Acta Mater. 61 (2013) 2628–2638.
[4] K. Jin, C. Zhang, F. Zhang, H. Bei, Influence of compositional complexity on interdiffusion in Ni-containing concentrated solid solution alloys, Mater. Res. Lett. 6 (5) (2018) 293–299.
[5] D.B. Miracle, O.N. Senkov, A critical review of high entropy alloys and related concepts, Acta Mater. 122 (2017) 448–511.
[6] A.G. De La Torre, A. Cabeza, A. Calvente, S. Bruque, M.A.G. Aranda, Full phase analysis of Portland clinker by penetrating synchrotron powder diffraction, Anal. Chem. 73 (2001) 151–156.
[7] A.R. Yavari, J.F.R. De Castro, G. Vaughan, G. Heunen, Structural evolution and metastable phase detection in MgH –5%NbH 2 nanocomposite during in-situ H-desorption in a synchrotron beam, J. Alloys Compd. 353 (2003) 246–251.
[8] F.F. Dismore, Computer searching of the JCPDS powder diffraction file, Adv. X-Ray Anal. 20 (1976) 113–123.
[9] B.D. Cullity, S.R. Stock, Elements of X-Ray Diffraction, Prentice hall, Upper Saddle River, NJ, 2001.
[10] S. Gates-Rector, T. Blanton, The powder diffraction file: a quality materials characterization database, Powder Diffr. 34 (2019) 352–360.
[11] H.M. Rietveld, A profile refinement method for nuclear and magnetic structures, J. Appl. Crystallogr. 2 (1969) 65–71.
[12] H. Gasan, E. Lökçü, A. Ozcan, O.N. Celik, I. Celikyurek, M. Ulutan, Y. Kurtulus, Effects of Al on the phase volume fractions and wear properties in the AlxCoCrFeMoNi high entropy alloy system, Met. Mater. Int. 26 (2020) 310–320.
[13] C.R. Reynolds, Z. Herl, N.A. Ley, D. Choudhuri, J.T. Lloyd, M.L. Young, Comparing CALPHAD predictions with high energy synchrotron radiation X-ray diffraction measurements during in situ annealing of $Al_{0.3}$CoCrFeNi high entropy alloy, Materialia 12 (100784) (2020).
[14] R. Feng, M.C. Gao, C. Zhang, W. Guo, J.D. Poplawsky, F. Zhang, J.A. Hawk, J. C. Neuefeind, Y. Ren, P.K. Liaw, Phase stability and transformation in a light-weight high-entropy alloy, Acta Mater. 146 (2018) 280–293.
[15] M. Gao, B. Schneiderman, S.M. Gilbert, Z. Yu, Microstructural evolution and mechanical properties of nickel-base superalloy brazed joints using a MPCA filler, Metall. Mater. Trans. A 50 (2019) 5117–5127.
[16] B. Schneiderman, O. DeNonno, J. Klemm-Toole, Z. Yu, Ductile braze repairs for Ni-base superalloys using novel MPEA filler, Weld. J. 101 (3) (2022) 85s–95s.

[17] D. Bridges, S. Zhang, S. Lang, M. Gao, Z. Yu, Z. Feng, A. Hu, Laser brazing of a nickel-based superalloy using a Ni-Mn-Fe-Co-Cu high entropy alloy filler metal, Mater. Lett. 215 (2018) 11–14.
[18] B. Schneiderman, A.C. Chuang, P. Kenesei, Z. Yu, In-situ synchrotron diffraction and modeling of non-equilibrium solidification of a MnFeCoNiCu alloy, Sci. Rep. 11 (2021) 5921.
[19] Inconel Alloy 600 Technical Brochure, Special Metals Corporation, 2008.
[20] Alloy IN-738 Technical Data, The International Nickel Company.
[21] C.B. Dallam, B.K. Damkroger, Characterization of Welds, ASM Handbook Volume 6: Welding Brazing and Soldering 1993, pp. 248–269.
[22] J.N. DuPont, J.C. Lippold, S.D. Kiser, Welding Metallurgy and Weldability of Nickel-Base Alloys, John Wiley & Sons, Hoboken, N.J., 2009.
[23] ThermoCalc Software: about the TCS Ni-based Superalloys Database (TCNI), ThermoCalc Software, 2022.
[24] J. Belan, GCP and TCP phases presented in nickel-base superalloys, Mater. Today 3 (2016) 936–941.
[25] E. Nembach, G. Neite, Precipitation hardening of superalloys by ordered gamma-prime particles, Prog. Mater. Sci. 29 (1985) 177–319.
[26] A.K. Sinha, Topologically close-packed structures of transition metal alloys, Prog. Mater. Sci. 15 (2) (1972) 81–185.
[27] A.S. Wilson, Formation and effect of topologically close-packed phases in nickel-base superalloys, Mater. Sci. Technol. 33 (9) (2017) 1108–1118.
[28] S. Azadian, L.Y. Wei, R. Warren, Delta phase precipitation in Inconel 718, Mater. Charact. 53 (2004) 7–16.
[29] T. Yang, Y.L. Zhao, L. Fan, J. Wei, J.H. Luan, W.H. Liu, C. Wang, Z.B. Jiao, J.J. Kai, C.T. Liu, Control of nanoscale precipitation and elimination of intermediate temperature embrittlement in multicomponent high entropy alloys, Acta Mater. 189 (2020) 47–59.
[30] Q. Feng, T.K. Nandy, T.M. Pollock, Observation of a Ru-rich Heusler phase in a multicomponent Ni-base superalloy, Scr. Mater. 50 (2004) 849–854.
[31] B.H. Toby, R.B. VonDreele, GSAS-II: the genesis of a modern open-source all purpose crystallography software package, J. Appl. Crystallogr. 46 (2013) 544–549.
[32] A. Jain, S.P. Ong, G. Hautier, W. Chen, W.D. Richards, S. Dacek, S. Cholia, D. Gunter, D. Skinner, G. Ceder, K.A. Persson, Commentary: the materials project: a materials genome approach to accelerating materials innovation, APL Mater. 1 (1) (2013), 011002.
[33] P. Strunz, M. Petrenec, V. Davydov, J. Polák, P. Beran, Misfit in inconel-type superalloy, Adv. Mater. Sci. Eng. (408347) (2013), 2013.
[34] D. Hicks, M.J. Mehl, E. Gossett, C. Toher, O. Levy, R.M. Hanson, G. Hart, S. Curtarolo, The AFLOW library of crysallographic prototypes: part 2, Comput. Mater. Sci. 161 (2019) S642.
[35] E.O. Hall, S.H. Algie, The sigma phase, Metall. Rev. 11 (1) (1966) 61–88.
[36] B. Schneiderman, A. Hansen, A.C. Chuang, Z. Yu, Influence of oxygen on performance of multi-principal element alloy as braze filler for Ni-base alloys, J. Manuf. Process. 87 (2023) 25–35.
[37] S.K. Gupta, Peak decomposition using Pearson type VII function, J. Appl. Crystallogr. 31 (1998) 474–476.
[38] T. Ida, M. Ando, H. Toraya, Extended pseudo-Voigt function for approximating the Voigt profile, J. Appl. Crystallogr. 33 (2000) 1311–1316.
[39] S.R. Shatynski, The thermochemistry of transition metal carbides, Oxid. Metals 13 (2) (1979) 105–118.
[40] N.I. Medvedeva, D.C. Van Aken, J.E. Medvedeva, Stability of binary and ternary M23C6 carbides from first principles, Comput. Mater. Sci. 96 (2015) 159–164.